ELSEVIER

Contents lists available at ScienceDirect

Journal of Power Sources

journal homepage: www.elsevier.com/locate/jpowsour



Probing lithiation and delithiation of thick sintered lithium-ion battery electrodes with neutron imaging



Ziyang Nie^a, Patrick McCormack^a, Hassina Z. Bilheux^b, Jean C. Bilheux^b, J. Pierce Robinson^a, Jagjit Nanda^c, Gary M. Koenig Jr.^{a,*}

- ^a Department of Chemical Engineering, University of Virginia, 102 Engineers Way, Charlottesville, VA, 22904-4741, USA
- ^b Oak Ridge National Laboratory, Neutron Scattering Division, 1 Bethel Valley Road, Oak Ridge, TN, 37831, USA
- ^c Oak Ridge National Laboratory, Chemical Sciences Division, 1 Bethel Valley Road, Oak Ridge, TN, 37831, USA

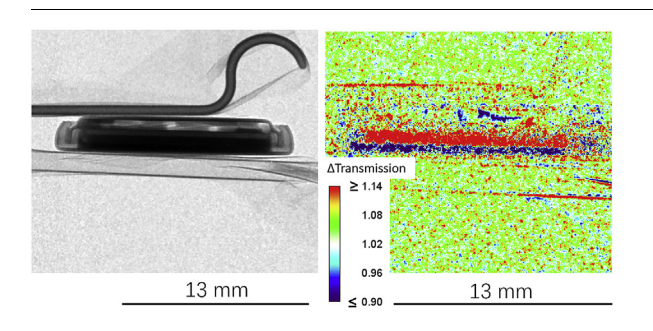
HIGHLIGHTS

- Characterizing electrochemical performance and limits of sintered electrodes.
- Neutron imaging to track lithiation/ delithiation throughout lithium-ion full cell
- Matching of calculated and experimental polarization and lithium profiles.
- Qualitatively different intercalation profiles for different thickness electrodes.

ARTICLEINFO

Keywords:
Neutron imaging
Lithium-ion battery
Sintered electrode
Ion transport
In situ characterization

GRAPHICAL ABSTRACT



ABSTRACT

As lithium-on (Li-ion) batteries increase in their prevalence and the range of applications expands, there is a need to understand and exploit the limits of electrochemical performance. Probing the internal processes in Li-ion batteries provides insights into the electrochemical characteristics of the cells as well as information necessary for rational cell design. In this manuscript an *in situ* method, neutron imaging, is applied to Li-ion full cells to track the lithiation/delithiation processes in the electrodes during discharge. The electrodes comprise thick sintered films of only active material, which improves the number of discrete points that are mapped for net changes in neutron intensity through the electrode. The lithiation/delithiation processes are qualitatively consistent with calculations of the Li⁺ concentration and discharge profiles of the cells. These results illustrate that neutron imaging can experimentally probe and confirm limitations in the electrochemical performance of Li-ion full cells, particularly those with thick electrodes.

1. Introduction

Lithium-ion (Li-ion) batteries have become a critical technology for many applications, including consumer electronics and electric vehicles [1,2]. Understanding the material and performance limits of different

Li-ion materials and components requires an understanding of how they function while being electrochemically charged and discharged. A variety of techniques have been developed to probe the operating fundamentals at different lengths scales – for example in-situ transmission electron microscopy electrochemical cells can provide insights

E-mail addresses: zn3ga@virginia.edu (Z. Nie), pm4ty@virginia.edu (P. McCormack), bilheuxhn@ornl.gov (H.Z. Bilheux), bilheuxjm@ornl.gov (J.C. Bilheux), jpr6su@virginia.edu (J.P. Robinson), nandaj@ornl.gov (J. Nanda), gary.koenig@virginia.edu (G.M. Koenig).

^{*} Corresponding author.

into very local changes within the surface and bulk of electroactive materials during lithiation/delithiation [3]. Other techniques such as high resolution x-ray diffraction provide detailed structural information during electrochemical processes, but generally average that information using contributions from a larger amount of material within the cell [4]. While the techniques described above provide insights into processes and changes occurring with the electroactive material, it can be challenging to derive insights into the impacts, if any, of the transport of Li⁺ ions through the porous architecture of the battery electrodes. In some cases, for example when electrodes are relatively thick, transport of Li + through the porous electrode (and separator) architecture can limit the charge/discharge rate [5,6]. For electrodes or battery cells that are limited, or potentially limited, by these processes of Li⁺ transport through the porous void regions filled with electrolyte, tracking the transport and distribution of Li + in situ during the charge and discharge processes is critical to understand the transport occurring within the cell.

Towards the goal of tracking the in situ distribution of and/or transport of Li⁺ within a battery cell, a number of techniques have been deployed. Recently, x-ray phase imaging was employed to quantify and visualize salt concentration distributions in battery electrolytes [7]. This technique provides quantitative concentration profiles of the Li⁺ in the electrolyte, but a specialized spectroelectrochemical cell was required and access to concentration information was restricted to between the electrode regions. X-ray tomography has also been used to visualize the distribution of conversion electrode materials in situ [8], although more subtle compositional changes such as the electrolyte concentration profile and the lithiation/delithiation of intercalation materials is more challenging using this method. More recently, there have been a few reports of using neutron imaging to track the distribution of Li⁺ within a Li-ion cell. The transmission of the neutrons is highly sensitive to the total amount of Li + (and more specifically the ⁶Li⁺) the neutrons interact with as they pass through the cell to the detector [9,10], and thus neutron radiographs have high sensitivity to Li + compositional changes in a battery cell. For example, the lithiation of a graphite cathode was quantitatively tracked in situ using neutron radiographs of a pouch cell [9]. In addition, neutron tomography can be used to determine the three-dimensional distribution of lithiation/delithiation of active material, although the timescale of image collection generally limits the cells to post cycling analysis or extremely low rates of charge/discharge [11].

Although neutron imaging has the advantages of being highly penetrating which enables not having to assemble special custom cells for analysis, and highly sensitive to Li+ which enables tracking the entire active region of both electrodes and the electrolyte, a report in the literature of a Li-ion battery full cell with two intercalation electrodes undergoing neutron imaging in situ during electrochemical charge or discharge has been lacking. One of the primary reasons for this is the resolution of the technique - with previous reports having pixel sizes of $\sim 40 \ \mu m$ and resolution of $\sim 75 \ \mu m,$ though resolution can be improved with the tradeoff of significant reductions in field of view [9]. This resolution and pixel size limits the number of thickness locations that can be independently assessed within the cell or electrodes, because electrode thicknesses for Li-ion batteries are frequently 100 µm or less [12]. However, recently there have been reports of Li-ion battery cells with thicker electrodes, in some cases many hundreds of micrometers thick [13,14]. The thick electrodes are produced via hydraulic pressing and sintering, which results in pores in the electrode free of inactive binder and conductive additive components and the lack of a more conventional composite electrode architecture removes the concern of electrode delamination. The use of a full cell with two intercalation electrodes mitigates the current density, thickness change, and cycling limitation complications of having one of the electrodes be lithium metal [13]. Herein, neutron imaging will be used to quantify the lithiation/delithiation processes of a Li-ion battery full cell, where the electrodes are comprised of sintered porous thin films of intercalation

materials. The neutron radiographs will be evaluated in the context of simulations of ${\rm Li}^+$ concentration profiles calculated using a porous electrode model [15–17].

2. Materials and methods

2.1. Preparation of active material powders

 ${\rm Li_4Ti_5O_{12}}$ (LTO) active material powder used in the anode was purchased from a commercial supplier (NANOMYTE BE-10 from NEI Corporation). LiCoO₂ (LCO) powder used as the active material in the cathode was synthesized using previously reported procedures based on the co-precipitation of ${\rm CoC_2O_4}{:}2{\rm H_2O}$ precursor and calcination with ${\rm Li_2CO_3}$ salt in a furnace with an air atmosphere [18]. For the LCO synthesis, in brief:

Cobalt oxalate precursor was synthesized using $1800\,\text{mL}$ $62.8\,\text{mM}$ $\text{Co(NO}_3)_2\text{-}6\text{H}_2\text{O}$ (Fisher Reagent Grade) and $1800\,\text{mL}$ $87.9\,\text{mM}$ $(\text{NH}_4)_2\text{C}_2\text{O}_4\text{H}_2\text{O}$ (Fisher Certified ACS) first prepared as separate solutions using deionized water, and both were heated to $50\,^{\circ}\text{C}$. Then, Co $(\text{NO}_3)_2\text{-}6\text{H}_2\text{O}$ solution was poured into $(\text{NH}_4)_2\text{C}_2\text{O}_4\text{-}\text{H}_2\text{O}$ solution all at once. The solution was stirred at $800\,\text{rpm}$ and maintained at $50\,^{\circ}\text{C}$ for $30\,\text{min}$. After that, the solid precipitate product was collected using vacuum filtration and rinsed with $4\,\text{L}$ deionized water. The powder was dried in an oven exposed to the surrounding air atmosphere for $24\,\text{h}$ at $80\,^{\circ}\text{C}$.

To convert the precursor to LCO final active material, the oxalate particles were mixed with $\rm Li_2CO_3$ (Fisher Chemical) powder with a Li:Co ratio of 1.02:1. The mixture was calcined in Carbolite CWF 1300 box furnace under an air atmosphere by heating to 800 °C with a ramp rate of 1 °C min $^{-1}$. Upon reaching the target temperature of 800 °C, the heat supplied to the furnace was turned off and it was allowed to cool to ambient temperature without any control over the cooling rate. The resulting LCO material was ground by hand using mortar and pestle and was further milled using Fritsch Pulverisette 7 planetary ball mill. For the ball milling, LCO powder was mixed with 5 mm diameter zirconia beads and milled for 5 h at 300 rpm. The detailed materials characterization of the LTO and LCO materials used in this study, as well as their electrochemical characterization in conventional composite electrodes, can be found in previous reports [13,18,19].

2.2. Electrode preparation and battery fabrication

The electrodes used in neutron imaging experiments were porous sintered metal oxides that were comprised of only active material. Cathode and anode pellets were independently and separately prepared using the same procedure. First, 1 g active powder was mixed with 2 mL 1 wt% polyvinyl butyral (Pfaltz& Bauer) dissolved in ethanol (Acros). Mortar and pestle were used to facilitate mixing the slurry, and the hand mixing was continued until all solvent was evaporated. Second, the mixture powder was loaded into a 13 mm Carver pellet die. For the cell with "thin" electrodes, 0.2 g powder was used for LCO and 0.22 g powder was used for LTO. For the cell with "thick" electrodes, 0.26 g powder was used for both anode and cathode. For all pellets, the powder was pressed within the pellet die with 12.000 lb_f for 2 min in a Carver hydraulic press. The pellets were carefully extracted from the die intact and were sintered in a Carbolite CWF 1300 box furnace under an air atmosphere. The program used consisted of ramping from 25 °C to 700 °C at 1 °C min⁻¹, holding at 700 °C for 1 h, then cooling to 25 °C

The electrodes, comprised of porous disks containing only sintered electroactive materials, were assembled into full cells within CR2032 coin cells. The LCO pellets were attached to the bottom plate of the cell (Fig. 1a) using carbon paste (1:1 wt ratio Super P carbon black (Alfa Aesar) to polyvinylidene difluoride (PVDF, Alfa Aesar) binder dissolved in N-methyl pyrrolidone (NMP, Sigma-Aldrich)) and dried for 12 h in an oven in air at 80 °C. The LTO pellets were pasted on the stainless steel

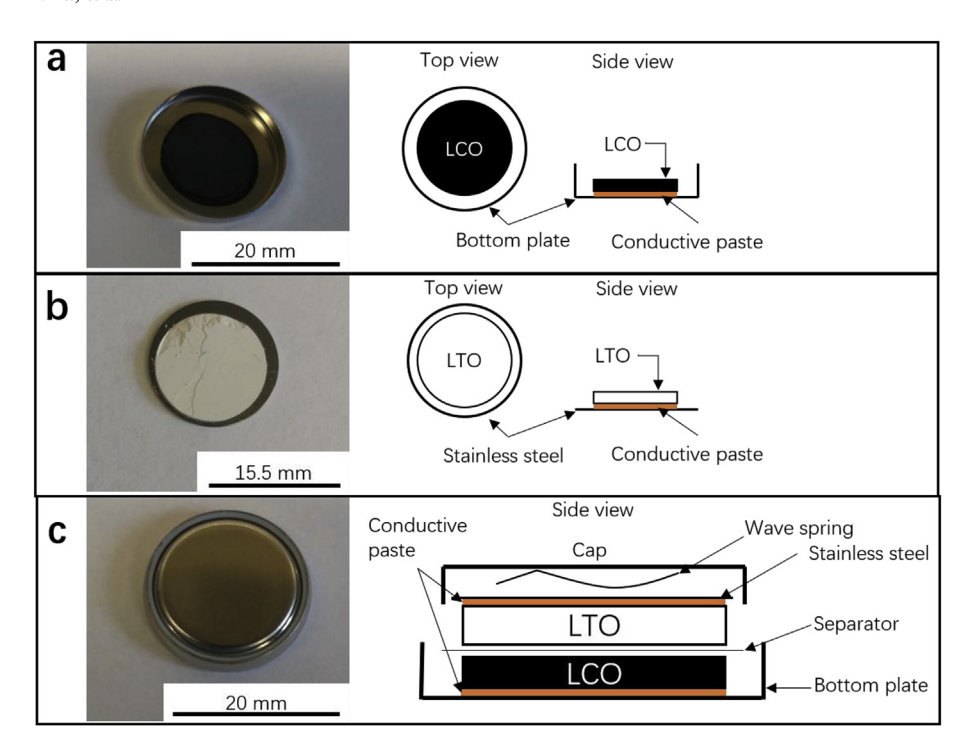


Fig. 1. (left) Photographs and (right) cartoon schematics depicting the different components and assembly of a CR2032 coin cell where both electrodes were sintered pellets. (a) Bottom plate with LCO pellet pasted within. (b) Spacer with LTO pellet pasted on top (note that LTO used in picture has noticeable cracks/defects on surface, while those used in cycled cells did not). (c) Final assembled coin cell (note that electrolyte and gasket are not shown in the schematic).

spacer of the coin cell using the same paste and drying procedure (Fig. 1b). The pellets attached to stainless steel were then transferred into an Ar-filled glove box (O_2 and H_2O both < 1 ppm) for the remaining coin cell assembly steps. LTO and LCO electrodes were paired together while separated by a Celgard 2325 polymer separator. 16 drops of electrolyte (1.2 M LiPF₆ in 3:7 ethylene carbonate:ethyl methyl carbonate, purchased from BASF) were added. Other coin cell parts to complete assembly included a stainless steel wave spring, a stainless steel top cap, and a Teflon gasket (Fig. 1c). As described above, a "thin" cell and a "thick" cell were assembled for evaluation, where the sintered electrodes were used for LTO/LCO full cells. The LTO/LCO-Thin cell had electrodes with thicknesses of 0.738 mm and 0.463 mm for LTO and LCO, respectively. The LTO/LCO-Thick cell had electrodes with thicknesses of 0.886 mm and 0.640 mm for LTO and LCO, respectively. Representative scanning electron micrographs (SEMs, FEI Quanta 650) of LCO and LTO sintered pellet electrodes can be found in the Supporting Information, Fig. S1.

The coin cells were cycled galvanostatically at different C rates, where the C rate was based on the mass of LCO in the cell with an assumed capacity of 150 mAh g $^{-1}$ LCO (e.g. 1C was assumed to be 150 mA g $^{-1}$ LCO). Electrochemical cycling was performed using a MACCOR battery cycler or Bio-Logic potentiostat, with the Bio-Logic used for all electrochemical cycling conducted concurrent with neutron imaging. The cut off voltage limits were 1.0 V–2.8 V for all cells and C rates evaluated.

2.3. Neutron imaging

The neutron imaging experiment was carried out at the High Flux Isotope Reactor CG-1D beamline at Oak Ridge National Laboratory (ORNL) [20]. A photograph showing the experimental setup with the coin cells in front of the scintillator detector can be found in Fig. 2a. An example of the raw radiograph taken of the cells in Fig. 2a can be found in Fig. 2b. To achieve sufficient neutron collection, each image was collected over a 35 s duration. This timescale was much shorter than the fastest discharge cycle that will be discussed in this report (for the fastest discharge each radiograph represents < 0.07% of the total discharge time) which gave confidence that the image collection timescale gave sufficient temporal resolution for the processes being investigated.

The raw radiograph was normalized using open beam and dark field corrections, and an example of a normalized transmission radiograph of the cells from the same experiment in Fig. 2b can be found in Fig. 2c. The goal of the neutron imaging was to track net changes in lithium concentration throughout the thickness of the cell during cycling, and thus the image data that will be discussed in the manuscript was further normalized relative to images collected before starting cycling (relative to the "no current" image). This normalization resulted in the cell components outside of the electrode region being approximately transparent because they were unchanged, while significant dark and bright contrast resulted in the electrode regions due to net Li + movement and Li+ concentration changes. Darker regions correspond to lower transmission while brighter regions correspond to higher transmission relative to before cycling was initiated. Lithium was responsible for the majority of the attenuation (and thus decreases in neutron transmission) in the sample, and thus darker regions correspond to increased Li+ concentration, while brighter regions correspond to decreased Li+ concentration within the cell electrodes (relative to before cycling was initiated). In neutron images (normalized to "no current") where grayscale is used, the dark/light contrast indicates net Li+ concentration change as described above. In other cases a color scale for the changes in transmission was used to show the distribution of changes in neutron transmission throughout the electrodes (see Fig. 2d, which is the adjusted image of the red box region in Fig. 2c, after normalizing relative to the no current image and using a color scale). The sample image in Fig. 2d was from the time point at the end of the C/30 discharge, which was chosen to illustrate the clear contrast between anode and cathode region with the net migration and insertion/ deinsertion of Li⁺ from the respective electrodes. In Fig. 2d, the electrode on the bottom (blue region) is LCO which has increased Li+ concentration because the cell has been partially discharged and correspondingly the electrode on the top (red region) is LTO which has had a net decrease in Li+ concentration. To extract the quantitative transmission information and maps of gradients in the z-direction in the cell (see Fig. 2d for z-direction), a 200-pixel wide line scan was used across the electrode area from bottom to the top. For both the LTO/LCO-Thin and LTO/LCO-Thick cells, the cells were charged to 2.8 V at a rate of C/ 100 before being shipped to ORNL. Then, after placing in the experimental setup in the neutron beam (Fig. 2a), the cells were charged

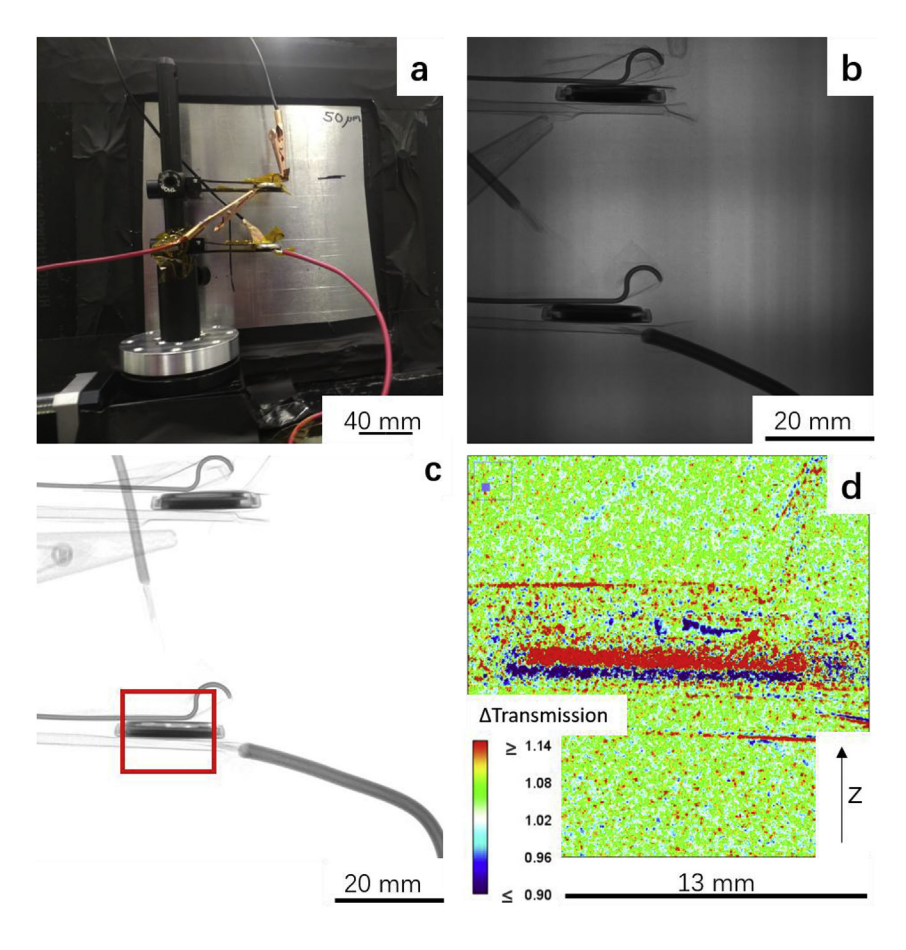


Fig. 2. (a) Photograph of neutron imaging experimental setup. Example neutron images depicting (b) raw collected radiographs, (c) transmission radiograph after normalizing using open beam and dark field radiographs, and (d) coin cell after normalizing relative to images collected before initiating cycling and adding a color scale that corresponds to the relative change in neutron transmission. The image area in (d) is the same region as the red boxed region in (c). Inset in (d) is a color scale bar with the numerical value corresponding to the changes in relative neutron transmission at each pixel relative to the initiation of discharge. Black arrow on bottom right corner of (d) depicts the z-direction in the experiment, which is the length/depth dimension that is the focus of the Li⁺ concentration profiles. Note that for (d) the brightest red regions have $\Delta T \ge 1.14$ and deepest blue regions have $\Delta T \leq 0.90$ and do not reflect the absolute maximum or minimum ΔT values. The color scale was truncated to best highlight the net change in the pixels throughout the electrode. (For interpretation of the references to color in this figure legend, the reader is referred to the Web version of this

again at a rate of C/50 to 2.8 V to recover any capacity that may have been lost to self-discharge during the 2 days between the charging at C/100 and the experiment at ORNL. Both cells were then discharged at a rate of C/30 while simultaneously collecting neutron radiographs. It is noted that due to exposure to the neutrons that some of the Co in the LCO becomes activated to ^{60}Co . ^{60}Co emits gamma rays and has a half-life of 5.27 years [21,22]. Thus, the cells used in the neutron imaging experiments cannot undergo post-testing materials characterization.

2.4. Model analysis

Experimental results were compared to calculations of electrochemical discharge of the cells conducted using the Dualfoil electrochemical model developed by Newman et al. [23]. In particular, the Li⁺ concentration profiles as a function of depth within the cell for both the liquid and the solid phase were extracted at different durations of discharge using the model, to compare to transmission profiles in the neutron radiographs. Details of the model have been discussed in previous publications [15–17,24]. A brief introduction to the model can be found in Supporting Information.

3. Results and discussion

3.1. Neutron radiographs during discharge of thin cell

After charging the cell to 2.8 V, the LTO/LCO-Thin sintered electrode battery was discharged to $1.0\,\mathrm{V}$ at a rate of C/30. This rate corresponds to $0.98\,\mathrm{mA}$ and $0.74\,\mathrm{mA\,cm}^{-2}$. The discharge voltage as a function of time can be found in Fig. 3a, and the total capacity delivered was 22.0 mAh, or $16.6\,\mathrm{mAh}$ cm⁻². LCO typically has a gradually sloping potential profile between $3.9\,\mathrm{V}$ (vs. Li/Li⁺) and a cutoff voltage (typically < $4.5\,\mathrm{V}$, vs. Li/Li⁺) [25], while LTO has a flat charge/

discharge plateau at $\sim\!1.55\,V$ (vs. Li/Li⁺) [25], which would be expected to result in a sloping discharge curve between $\sim\!2.8\,V$ (the upper cutoff for the cells in this study) and $\sim\!2.4\,V$ [26]. As can be seen in Fig. 3a, the discharge profile has a gradual downward slope with the majority of the capacity between 2.5 V and 1.5 V. This discharge curve was consistent with an LTO/LCO cell, though with significant polarization. Thick sintered electrodes can have significant polarization due to the significant Li⁺ transport distances [13] and due to electronic conductivity and cell resistance limitations, which will be discussed in further detail in Section 3.3. The discharge profile and capacity at C/30 was consistent with previous reports for LTO/LCO sintered electrode battery cells [13].

Fig. 3b shows neutron radiographs taken at different points during the discharge of the LTO/LCO-Thin cell, with the color scale indicating the relative change in neutron transmission compared to just before discharge. At the initiation of discharge there was no significant change in pixel intensity in any region in the cell because the neutron transmission passing through different locations in the cell was not significantly different relative to the reference image taken before discharge. However, as the discharge proceeded, there was a clear red region that formed with a clear blue region below it, with a sharp step change between the two. The interface between the red and blue regions corresponded to the location of the separator between the LTO and LCO electrodes. The red region corresponded to the LTO electrode, and the blue region corresponded to the LCO electrode. As a function of discharge time/extent, the red region and blue region both extended further from the interface, though this was more noticeable with the red LTO top electrode. These changes in relative transmission were consistent with the net movement of Li⁺ within the cell. As the cell discharges, the total amount of Li⁺ within the electrolyte would be expected to stay constant (although the local concentration can vary significantly) [16]. However, during the discharge the LTO will be

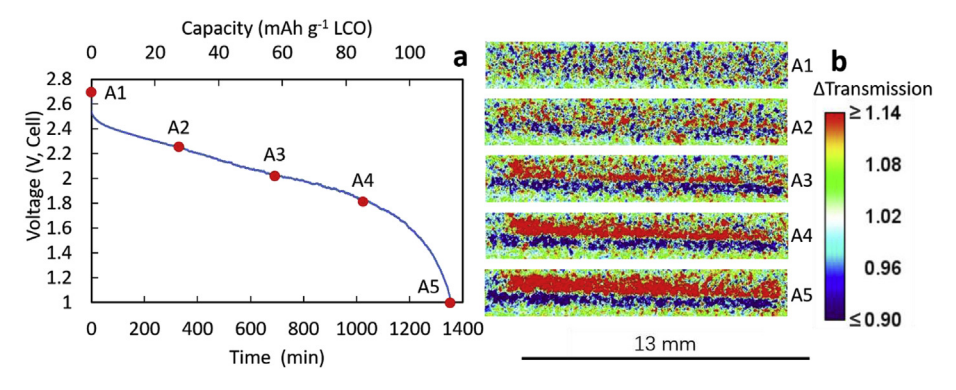


Fig. 3. (a) Discharge profile for the LTO/LCO-Thin cell. Time points A1-A5 are noted on the profile and correspond to the respective neutron images in (b). A1-A5 represent neutron radiographs that correspond to the times 0 min, 339 min, 678 min, 1017 min and 1357 min, respectively. The red and blue regions are the locations of the LTO and LCO electrodes, correspondingly. Inset in (b) is a color scale bar with the numerical value corresponding to the changes in relative neutron transmission at each pixel relative to the initiation of discharge. Note that for (b) the brightest red regions have $\Delta T \geq 1.14$ and deepest blue regions have $\Delta T \geq 0.90$ and do not reflect the absolute maximum or minimum ΔT values. The color scale was truncated to best highlight the

net change in the pixels throughout the electrode. (For interpretation of the references to color in this figure legend, the reader is referred to the Web version of this article.)

delithiated from $\text{Li}_{4+y}\text{Ti}_5\text{O}_{12}$ back to $\text{Li}_4\text{Ti}_5\text{O}_{12}$ and simultaneously Li_{1-} xCoO₂ will be lithiated to LiCoO₂. Using the cell capacity of 22.0 mAh and assuming that at the end of discharge that the anode was uniformly of the composition Li₄Ti₅O₁₂ and the cathode was of the composition LiCoO₂, this means that when considering only the solid active material in the electrode the total concentration change in the LCO cathode material was from 30.2 to $51.2 \, \text{mol} \, \text{L}^{-1}$ and the total concentration change in the anode LTO material was from 21.5 to 7.6 mol L⁻¹. This significant net concentration of Li+ increase in the cathode and decrease in the anode, coupled with the large attenuation of neutrons absorbed by Li atoms due to its extremely large absorption coefficient [9,10], resulted in the observed relative transmitted intensity changes in the neutron radiographs. The propagation of the changes in transmitted intensity from the separator towards the current collector, which provided the electrical path from the electrode to the external cell contacts (e.g., stainless steel components labeled in Fig. 1), as a function of the discharge time/extent (particularly in the LTO and less extreme for the LCO, as will be discussed in more detail in Section 3.3) indicated that Li⁺ insertion into the cathode and deinsertion from the anode initially occurred on the separator/electrolyte side and propagated towards the current collector. This observation suggests that the electrochemical process was limited by the transport of the Li⁺ through the porous electrode architecture, as has previously been described for thick electrode systems in general [27]. If the rate of lithiation/delithiation was limited by the solid state diffusion of Li⁺ into/out of the individual active material particles, as is often the case in conventional and thinner Li-ion electrodes [28], more uniform and gradual changes in transmitted intensity throughout the electrode thickness would be expected. It is noted that there was some heterogeneity in the transmitted intensity in the electrodes. For example, the red region consistent with delithiation of the LTO does not extend as far towards the current collector in the region on the far right at the end of discharge (see "A5" in Fig. 3b). The origins of this heterogeneity could be the result of multiple possibilities, including the heterogeneity of the LTO particles themselves, the temperature distribution during sintering of the electrode, and the stresses encountered and contact quality during processing the pellet into the coin cell. Understanding the causes of this heterogeneity will be the subject of future investigations.

3.2. Neutron radiographs during discharge of thick cell

The resulting discharge profile for the LTO/LCO-Thick cell can be found in Fig. 4a. The cell was charged to the same cutoff voltage of 2.8 V, discharged to the same cutoff voltage of 1.0 V, and was discharged at the same C rate of C/30 (though due to the higher loading the absolute current and current density was higher, at 1.26 mA and 0.95 mA cm $^{-2}$) as the LTO/LCO-Thin cell. The total capacity delivered was 17.2 mAh (12.9 mAh cm $^{-2}$). Note that this discharge capacity was 45.4% of the charge capacity of the cell, while for the LTO/LCO-Thin

cell 75.4% of the charge capacity available was delivered during C/30 discharge. The polarization was also significantly greater in the LTO/LCO-Thick cell, with an average discharge voltage of 1.89 V, compared to the 2.03 V of the LTO/LCO-Thin cell. The only difference in the processing and fabrication of the LTO/LCO-Thick cell relative to the LTO/LCO-Thin cell was the greater thickness of the sintered electrodes. This suggested that the increased polarization and decreased capacity utilization was due to the longer diffusion paths of Li⁺ through the tortuous electrodes in the LTO/LCO-Thick system [13]. A more detailed discussion to further support this outcome can be found in Section 3.4.

The resulting neutron radiographs taken from different times during the LTO/LCO-Thick cell discharge can be found in Fig. 4b. The LTO/ LCO-Thick cell images also appeared at the initiation of discharge to not have much variation in relative transmitted intensity, again due to there being no significant difference in neutron transmission relative to the cell before discharge. Careful inspection of the image sequence from B1-B5 results in qualitatively similar trends to the LTO/LCO-Thin cell; there was an interface of red/blue contrast that developed in the cell in the location near where the separator was located, and the blue and red regions both propagated away from the separator and towards the current collector. The red region (LTO electrode) was again on top and the blue region (LCO electrode) was again on the bottom, consistent with the net loss of Li $^{+}$ from LTO and gain of Li $^{+}$ by the LCO. The total thickness of the propagation of the red and blue regions, as well as the total change in contrast/attenuation, did not attain as great of an extent for the LTO/LCO-Thick system. This was consistent with the total extent of discharge being less, meaning that less total Li⁺ (as a function of that available) was transferred across the LTO/LCO cell. This observation was also consistent with Li+ transport through the electrode pores being the limitation to extracting the cell's capacity, as the ability of the Li+ to traverse the full distance of both electrodes was not successful at the C/30 rate.

3.3. LTO/LCO-thin cell ${\rm Li}^+$ composition comparison between experiment and calculation

To gain insights into the processes that limited the capacity and current density of the sintered electrode full cells, the Li⁺ intercalation/deintercalation from the electrodes as a function of the depth within the cells (e.g., z-direction thickness location, see Fig. 2d) was assessed using the neutron imaging profiles. To obtain the transmission profiles, the average of transmission profile of 51 vertical pixel profiles for the LTO/LCO-Thin cell (and 59 for the LTO/LCO-Thick cell) were used to aid in averaging out local fluctuations and heterogeneity. The depth was captured from a location slightly below the LCO electrode to a location slightly above the LTO electrode to ensure the entire region where Li⁺ concentration might change was sampled. For the LTO/LCO-Thin cell, this resulted in a sample region totaling 42 pixels (1430 µm). A neutron image highlighting the sample region can be found in the Supporting

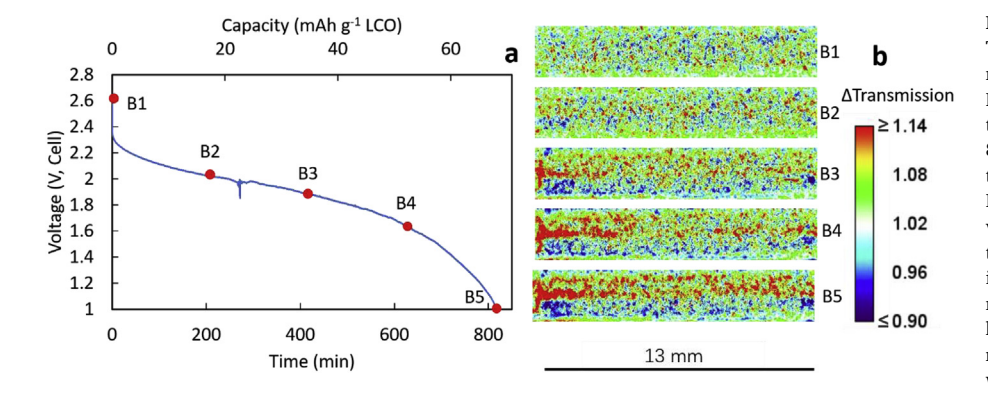


Fig. 4. Discharge profile for the LTO/LCO-Thick cell. Time points B1-B5 are noted on the profile and correspond to the respective neutron images in (b). B1-B5 are neutron radiographs that correspond to the times 0 min, 205 min, 409 min, 614 min and 819 min, respectively. The red and blue regions are the LTO and LCO electrode regions, correspondingly. Inset in (b) is a color scale bar with the numerical value corresponding to the changes in relative neutron transmission at each pixel relative to the initiation of discharge. Note that for (b) the brightest red regions have $\Delta T \ge 1.14$ and deepest blue regions have $\Delta T \leq 0.90$ and do not reflect the absolute maximum or minimum AT values. The color scale was truncated to best highlight the net change in the pixels throughout the electrode. (For interpretation of the references to color in this figure legend, the reader is referred to the Web version of this article.)

Information, Fig. S2a (and the relative transmission using a color scale in Fig. S2b). The corresponding sample region analyzed for the LTO/ LCO-Thick cells can be found in Figs. S2c and d. The transmission profiles were fairly consistent across the "width" of the cells (for comparison of different locations see Supporting Information, Fig. S3), particularly in the LCO electrode region. As mentioned previously each pixel had been normalized relative to when the cells were first put in the path of the neutron beam after alignment (these profiles can be found in Supporting Information, Fig. S4a). However, the more appropriate comparison for the calculations was the change in transmission relative to the initiation of discharge (see Supporting Information, Fig. S4b, the impact of this change was relatively minor). Also, for easier comparison to calculations, the depth location in the cell was normalized by finding regions where the transmission did not change and assuming those areas represented the locations of the anode and cathode current collectors (also depicted in Supporting Information, Fig. S4b). After these data processing steps, the resulting profiles represented the change in neutron transmission relative to that observed at the initiation of the experiment as a function of the normalized depth between 0 and 1, where 0 represents the edge of the LCO electrode in contact with the current collector and 1 represents the location of the LTO electrode in contact with the current collector. The resulting transmission profile for the LTO/LCO-Thin electrode can be found in Fig. 5a.

The change in transmission (ΔT) profiles as a function of time/extent of discharge for the LTO/LCO-Thin cell shown in Fig. 5a have a number of important features. First, overall the LCO electrode has a decrease in transmission and the LTO electrode has an increase in transmission relative to the initiation of discharge - this was consistent with the Li⁺ net traversing from the LTO electrode to the LCO electrode during discharge. The LCO side has an approximately parabolic profile, with the bottom of the curve shape getting progressively lower as the discharge proceeds. This progression was consistent with a relatively uniform lithiation of the LCO electrode as a function of depth. It was suspected that the parabolic shape resulted from a combination of 1) the averaging of the transmission of the neutrons over multiple regions of the cell with each pixel due to the relatively large pixel size and 2) slight misalignment of the cell in the beam (collectively, contributions from outside the LCO electrode regions). Both of these effects would result in a parabolic profile, because at the current collector there would be no change in transmission expected, and near the separator the transmission would be expected to change in the opposite direction, thus averaging with those regions would result in the net parabolic profile. On the LTO side, uniform delithiation would be expected to also result in a parabolic shape due to contributions from outside the electrode region that was inverted relative to the LCO electrode because the LTO experienced deintercalation and loss of the highly attenuating Li⁺. However, while the final state of the LTO electrode approximately

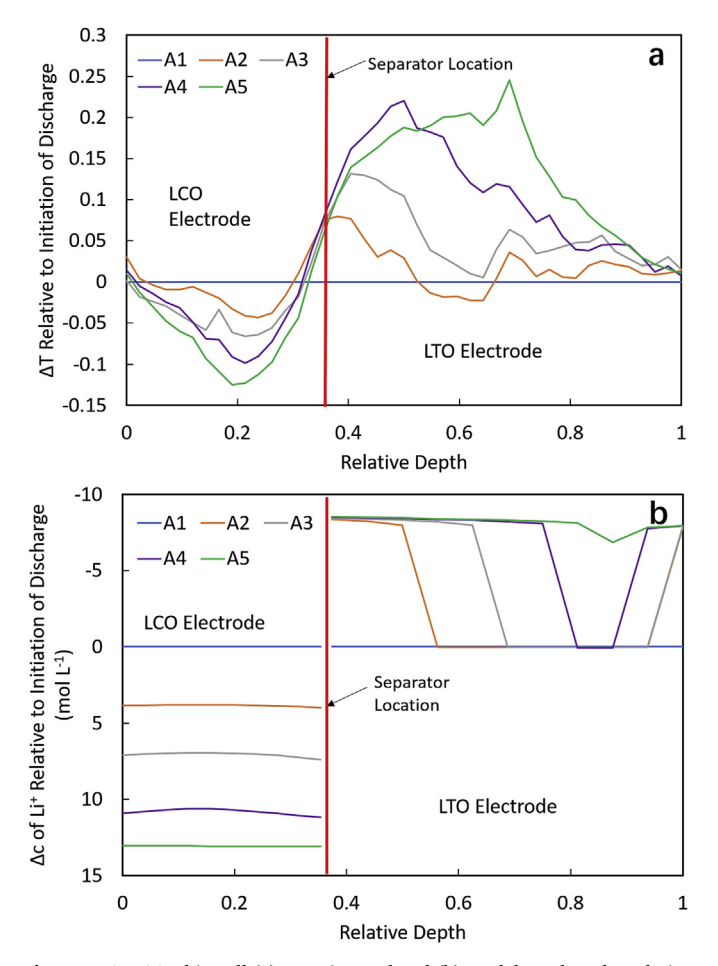


Fig. 5. LTO/LCO-Thin cell (a) experimental and (b) model results. The relative depth on the x-axis is the same for (a) and (b), and represents the thickness region normalized between the two electrodes (e.g., 0 is the connection of the LCO electrode to the current collector and 1 is the edge of the LTO electrode in contact with the current collector). Change in relative transmission intensity (Δ T) was determined from the neutron images collected during discharge for the A1-A5 timepoints corresponding to Fig. 3. Change in transmission intensity was relative to the image taken at the initiation of discharge (A1). Calculated change in Li⁺ concentration (Δ c) represents the difference between the total Li⁺ concentration at that depth compared to the total concentration at the initiation of discharge (A1).

resembled this outcome, the intermediate transmission profiles show a clear propagation of a transmission front from near the separator towards the current collector. This front suggested the Li⁺ was removed

 Table 1

 Battery parameters used in discharge calculations.

Parameters	LTO/LCO-Thin	LTO/LCO-Thick	Source
Thickness of negative electrode/LTO (m)	7.38×10^{-4}	8.66×10^{-4}	Measured
Thickness of separator (m)	2.5×10^{-5}	2.5×10^{-5}	Manufacturer
Thickness of positive electrode/LCO (m)	4.63×10^{-4}	6.40×10^{-4}	Measured
Bulk LiPF ₆ concentration (mol m ⁻³)	1200	1200	Manufacturer
Initial stoichiometric parameter, y for anode (y in Li _(4/3+y) Ti _(5/3) O ₄)	0.64	0.39	Estimate from experimental capacities
Initial stoichiometric parameter, x for cathode (x in Li _x CoO ₂)	0.58	0.75	Estimate from experimental capacities
Solid-state Li ⁺ diffusion coef. in anode (m ² s ⁻¹)	1×10^{-12}	1×10^{-12}	Experimental data and Ref. Zaghib et al. [32]
Solid-state Li ⁺ diffusion coef. in cathode (m ² s ⁻¹)	5×10^{-19}	5×10^{-19}	Ref. Geng et al. [33]
Radius of anode active particles (m)	1.7×10^{-7}	1.7×10^{-7}	Ref. Qi et al. [19]
Radius of cathode active particles (m)	1.5×10^{-7}	1.5×10^{-7}	Ref. Qi et al. [18]
Volume fraction of electrolyte in negative electrode	0.4	0.39	Based on measured porosity
Volume fraction of electrolyte in separator	0.39	0.39	Manufacturer
Volume fraction of electrolyte in positive electrode	0.36	0.31	Based on measured porosity
Conductivity of negative matrix (S m ⁻¹)	2	2	Ref. Young et al. [31]
Conductivity of positive matrix (S m ⁻¹)	0.3	0.3	Ref. Menetrier et al. [30]
Coulombic gravimetric capacity of negative material (mAh g ⁻¹)	175	175	Ref. Nitta et al. [25]
Coulombic gravimetric capacity of positive material (mAh g ⁻¹)	274	274	Ref. Nitta et al. [25]
Density of negative insertion material (kg m ⁻³)	3485	3485	Theoretical crystal density, Ref. Kataoka et al. [34]
Density of positive insertion material (kg m ⁻³)	5010	5010	Theoretical crystal density, Ref. Takahashi et al. [35]
Rate constant for negative reaction	8.7×10^{-6}	8.7×10^{-6}	Calculated based on Ref. He et al. [36]
Rate constant for positive reaction	4.3×10^{-7}	4.3×10^{-7}	Ref. Zhang et al. [37]
Internal resistance (Ω·m²)	6.3×10^{-3}	1.6×10^{-2}	Experimental data
Bruggeman exponent	1.5	1.5	Assumed consistent with literature. Ref. Fuller et al. [16]

from the LTO electrode in a much less uniform manner relative to the LCO electrode's intercalation with Li⁺, where the LTO contributing the Li⁺ during discharge started near the separator and came from progressively greater depths in the electrode as a function of time/extent.

To gain further insights into the Li⁺ distribution during the discharge of the LTO/LCO-Thin cell, calculations were performed using concentrated solution theory applied to the porous electrode model, as developed by Newman et al. [15-17]. The relevant conservation equations can be found in the Supporting Information. A number of parameters were needed for the model, and they were either measured directly, found in the relevant literature, or assumed using approximations previously developed for the model. The detailed list of parameters can be found in Table 1. There have been multiple applications of this model using composite electrodes [16,29], and two of the major differences that must be accounted for when using the sintered electrodes relative to the composite electrodes were that 1) the particles were not individually dispersed in the electrode and 2) the matrix conductivity in the electrode must come from the electroactive porous film itself rather than the carbon black/binder composite. For the first item, because the particle sintering was fairly mild (see Supporting Information, Fig. S1 for surface morphology) it was still assumed that the initial average particle size of the active material powders could be used for the electroactive particle diameters. For the second item, it was assumed that literature reports of the electronic conductivity after slight lithiation of LTO and delithiation of LCO could be used as the matrix conductivity [30,31]. The as-synthesized electronic conductivities of these materials were much lower, however with slight delithiation of LCO [30] and lithiation of LTO [31] the electronic conductivity as reported in the literature significantly increased, particularly for LTO. The cells that were used had already been cycled a few times, meaning there should have been residual loss of Li⁺ from LCO and gain of Li⁺ by LTO even though the cell was fully charged at the beginning of the experiment. Using these conductivities also ignores resistance at grain boundaries, thus the electronic conductivities used likely represent a relatively high approximation. It is noted that calculations where the matrix conductivity was intentionally decreased for LTO and LCO electrodes did not impact the results interpretation until the conductivity was decreased by over two orders of magnitude, indicating there was a reasonable margin for the matrix electronic conductivities chosen. It is also noted that the cell internal resistance, extracted from experimental impedance spectroscopy measurements on

the cells, were also quite high relative to conventional coin cells. It was suspected that this was due to resistance from the conductive paste and the quality of the contacts between the paste and both the sintered electrodes and the current collector.

The simulated LTO/LCO-Thin cell discharge had a capacity of 20.3 mAh, in close agreement with the experimental value (the calculated and experimental discharge profiles can be found in the Supporting Information, Fig. S5). While the discharge capacity/time matched well, there was significantly more polarization in the experimental profile. It is suspected that the assumption on the matrix conductivity was one of the main simplifications that made the polarization difficult to match more quantitatively, because as the cell discharges the electronic conductivity could change significantly as a function of both depth and time. With the calculation, the Li+ composition as a function of cell depth can be determined for both the liquid electrolyte phase and the solid electroactive material phase, as well as the sum of these concentrations (the calculated concentrations for the LTO/LCO-Thin cell can be found in Supporting Information, Fig. S6). The Li⁺ concentration changes in both the liquid and solid phase will contribute to the resulting neutron transmission changes during discharge, however, the greatest calculated change in Li^+ in the liquid phase was < 0.4 mol L^{-1} (see Fig. S6a), while the change in the solid phase was > 10mol L⁻¹ in both electrodes (see Fig. S6b), and both phases occupy a similar volume fraction within the electrode. It is also noted that every constituent in the cell will contribute to the attenuation of the neutrons, however, the change in transmitted intensity relative to the initiation of discharge will only reflect changes in the dimensions of the cell components, which were expected to be negligible relative to the resolution of the neutron imaging, and changes in the composition within the cell. Other elements such as Co and Ti, while attenuating to neutrons, were not expected to have net transport that would change their compositional density within the cell to measurably impact the neutron radiographs. The change in Li⁺ concentration (Δc) was calculated relative to the beginning of discharge, and the electrode depth was normalized by the total thickness, to make comparison of the calculated Li + profiles to the experimental neutron transmission profiles more straightforward.

The calculated change in ${\rm Li}^+$ concentration through the cell thickness can be found in Fig. 5b. The ${\rm Li}^+$ concentration scale has been inverted with increasing ${\rm Li}^+$ going down instead of up to make comparison with the changes in neutron transmission more straightforward because decreased transmission corresponded with increased ${\rm Li}^+$. The

increase in the Li+ concentration in the LCO electrode was uniform in the calculation across the LCO electrode thickness, with the extent of lithiation gradually increasing for all of the LCO material throughout the electrode as the discharge progressed. This was consistent with neutron transmission profiles. As discussed above, the parabolic shape resulted from regions of the cell that had unchanged or increasing transmission due to alignment and pixel averaging challenges. The peak in the transmission of the LCO electrode does slightly shift toward the current collector in the experimental profiles (Fig. 5a) indicating that there may have been slightly more lithiation near the separator in the LCO electrode, but the shift was not dramatic. In contrast, the LTO electrode has a fairly sharp transition where there was a region that goes from the separator into the electrode that has been completely delithiated (e.g., profile "A2" in Fig. 5b), a steep gradient in the extent of delithiation moving closer to the current collector, and then an area through the rest of the electrode thickness until reaching the current collector that was still fully lithiated and had not participated in the cell discharge. This gradient region propagates towards the current collector as the discharge proceeds, maintaining distinct regions that are either fully lithiated or fully delithiated. Also, at extents/durations of discharge "A3" and "A4" there was a second gradient region that propagated from the current collector towards the separator - and both gradients eventually disappeared at the end of discharge when the LTO electrode was completely delithiated throughout its thickness. Experimentally, the neutron transmission profiles within the LTO electrode also had an obvious sharp gradient region that propagated from the separator towards the current collector as a function of discharge time/ extent. Such a gradient was consistent with Li+ transport through the electrodes limiting the rate of discharge, which was not surprising given the large thickness of the electrodes. For the LTO/LCO-Thin electrode, the delithiation initiating from the current collector side of the LTO electrode was not observed experimentally. Lithium deintercalation will occur in the electrode at the locations with the lowest polarization. Within the LTO electrode, regions near the separator have the lowest ion transport polarization, while regions near the current collector have the lowest electron transport polarization [38]. As the lithiation gradient moved closer to the current collector, the polarization associated with the Li+ moving all the way back to the separator (then subsequently through the current collector and LCO electrode) continued to increase. At some point the increased polarization due to ion transport associated with being even further from the separator in regions very near the current collector was balanced by the lower electronic resistance of being near the current collector, and the second delithiation front initiated near the current collector. While it was possible this occurred to an extent in the LTO/LCO-Thin cell, it was difficult to directly observe this second gradient in the neutron transmission profiles. This may have been due to limits in the experimental resolution, or may have also been due to the assumptions mentioned above on the matrix conductivity in the LTO electrode. If the LTO electronic conductivity of the matrix was effectively much higher, the second delithiation gradient initiating on the current collector side of the LTO electrode would not be expected.

3.4. LTO/LCO-thick cell Li⁺ composition comparison between experiment and calculation

The LTO/LCO-Thick cell was next analyzed for Li $^+$ intercalation/deintercalation during discharge. The transmission profiles during different discharge times/extents were processed using the same methods as described for the LTO/LCO-Thin cell (see Supporting Information, Figs. S7 and S8), and the results can be found in Fig. 6a. The thickness was again normalized from 0 to 1, with 0 being the LCO current collector and 1 being the LTO current collector, although for the LTO/LCO-Thick cell that total distance in the cell was 1836 μ m as opposed to 1430 μ m. Looking at the electrodes on the whole, the average transmission in the LCO electrode decreased, while in the LTO electrode

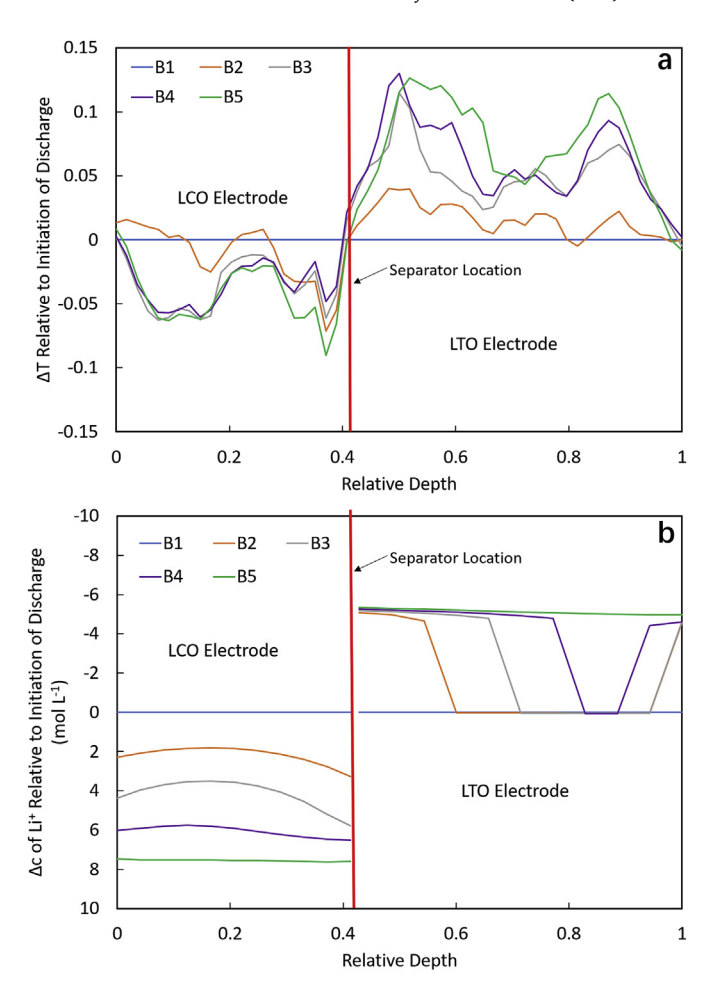


Fig. 6. LTO/LCO-Thick cell (a) experimental and (b) model results. The relative depth on the x-axis is the same for (a) and (b), and represents the thickness region normalized between the two electrodes (e.g., 0 is the connection of the LCO electrode to the current collector and 1 is the edge of the LTO electrode in contact with eh current collector). Change in relative transmission intensity (Δ T) was determined from the neutron images collected during discharge for the B1-B5 timepoints corresponding to Fig. 4. Change in transmission intensity was relative to the image taken at the initiation of discharge (B1). Calculated change in Li⁺ concentration (Δ c) represents the difference between the total Li⁺ concentration at that depth compared to the total concentration at the initiation of discharge (B1).

transmission increased, consistent with the net transfer of the highly attenuating Li⁺ during discharge to lithiating the LCO after delithiating the LTO. For the LCO electrode in the LTO/LCO-Thick cell, the lithiation does not appear to be as uniform. There are two distinct regions closer to the current collector and closer to the separator that have significant decreases in transmission, consistent with lithiation in those regions. However, the mid region of the electrode does not have as large of a decrease in transmission, suggesting there was more significant lithiation/discharge of the LCO material closer to the two edges of the electrode and less lithiation towards the middle of the electrode thickness. While there was greater extent of lithiation nearer the ends of the electrode, there was not an observable gradient that moved through the electrode (in either direction) like the LTO electrode in the LTO/ LCO-Thin cell case. Within the LTO electrode, there was a noticeable sharp gradient in the transmission profile that propagated from the separator towards the current collector, which was qualitatively consistent with the LTO/LCO-Thin cell. A new feature in the LTO/LCO-Thick cell LTO electrode, however, was a gradually increasing transmission near the current collector, suggesting delithiation in this region started fairly early during the discharge and Li + was extracted from this region as the discharge proceeded. The extent of the discharge of the LTO/LCO-Thick cell was much lower than the LTO/LCO-Thin cell (45.4% vs. 75.4%), thus the average net changes in transmission - increase in LTO electrode and decrease in LCO electrode – were lower for this cell.

The discharge of the LTO/LCO-Thick cell was also simulated using the same model as for the LTO/LCO-Thin cell (for calculated discharge profile see Supporting Information, Fig. S9). The calculated discharge profile had a capacity of 17.0 mAh, again in close agreement with the experiment. The only parameters that were changed relative to the LTO/LCO-Thin cell calculation was the thickness of each electrode was increased to match their measured values, the discharge current was increased such that both cells were discharged at C/30 on an LCO material mass basis, and the internal cell resistance that was used was the one measured for the appropriate cell. The simulated capacity of the cell matched very well to the experimentally observed value, although the experimental discharge curve had more polarization as was also the case for the thinner cell and was discussed above. The Li+ concentration profiles in the liquid and solid phase were again extracted from the calculation and summed (see Supporting Information, Fig. S10) and the change in total Li+ concentration was determined relative to the beginning of the discharge. The resulting calculated Li+ concentration profile through the cell thickness can be found in Fig. 6b for the LTO/ LCO-Thick cell. Overall, the Li $^{\scriptscriptstyle +}$ concentration increased in the LCO and decreased in the LTO as the discharge extent/time proceeds. In the LCO electrode, the lithiation was relatively uniform as a function of thickness, though for a couple of the profiles (e.g., "B3" at 409 min) there was a slight increase at the two edges of the electrode near the current collector and separator. The increased lithiation near the edges resulted in slightly less lithiation, which would increase the transmission, near the center of the LCO electrode thickness. The extent of the calculated underlithiation was not large enough to account for all of the observed lack of lithiation in the center region of the electrode, but the overall outcome of having relatively low electronic polarization near the current collector and ionic polarization near the separator was likely to play a role. Lithium being selectively deposited at both edge regions (near both the current collector and separator) has been previously reported in the literature for other battery systems, including lithiumair [39]. In the lithium-air case, the sluggish transport of Li+ on one side and O2 on the other resulted in peaks in discharge product (and hence Li⁺) concentration near the edges. It is suspected that in the observations in the sintered electrode with higher extent of discharge near the edges that it similarly reflected the two sluggish phenomena in the cell at high rates – with one being the transport of Li + and the other being the transport of electrons. The calculations and experimental profiles were both consistent with not having a lithiation gradient front that propagated through the LCO cathode, which was in contrast to the LTO anode.

The calculated delithiation of the LTO anode was qualitatively similar to that of the LTO/LCO-Thin cell. Initially a gradient propagated from the separator towards the current collector, where to the left of the front the LTO was completely delithiated and to the right of the front the LTO was all still lithiated, and there was a sharp gradient in Li + concentration in the transition region. At a later time (first observed in Fig. 6b at "B3" at 409 min) a second front of delithiation started which propagated from the current collector toward the separator, and at the end of the calculation almost all of the LTO in the electrode was uniformly delithiated. The transmission profile behavior for the LTO/LCO-Thick cell was very consistent with the calculation. There was a noticeable gradient in the transmission that propagated from the separator towards the current collector, consistent with a delithiation gradient that moved through the electrode, although the experimental delithiation gradient traversed through the electrode thickness more slowly. In addition, the "B3" 409 min transmission profile had a significant increase in transmission near the current collector, consistent with the calculation results. While it was not as clear in the

transmission profiles that the delithiation near the current collector also had a gradient that propagated towards the separator as was observed in the calculation, the relative transmission did increase as a function of discharge time/extent and the peak in transmission shifted slightly towards the separator. At the end of discharge, the calculated relative Li⁺ concentration profile was very uniform, while the experimental transmission profile had a significant decrease in transmission in the center region of the electrode, indicating the center of the LTO electrode did not achieve as complete of a delithiation. This suggested the end of the discharge resembled one of the calculated discharge profiles slightly before the end of discharge, where the two gradients had not converged together and there was a substantial region that had not been delithiated between the two. Thus, the difference between experiment and calculation for the delithiation in the center of the LTO electrode may indicate the extent of delithiation of the LTO as a whole was overestimated in the calculation.

The results presented in this manuscript demonstrate that insights into the lithiation/delithiation processes and transport limitations of Liion full cells can be obtained via in situ neutron imaging experiments using sintered electrodes. It is noted that translation of these results and insights to more commonly used composite Li-ion battery electrodes is not straightforward. While the sintered electrodes have void regions in the pore volume between active material particles which is filled with electrolyte, these same interstitial regions in a composite electrode also contain binder and conductive additives. The additional components result in much better electronic conductivity in the electrode relative to the sintered electrode system, but can significantly restrict the Li+ transport through the electrode architecture [40,41]. This transport limitation has been accounted for in some reports via correction to the Bruggeman scaling, but this correction has been very sensitive to the specific electrode composition and processing conditions [42,43]. In addition, the fundamental process which limits the performance of composite electrodes can be very dependent on the details of the active material chemistry and electrode chosen and many other cell factors. For example, Li+ and/or electron transport within the solid active material phase can limit the rate capability for electrodes with active material particles significantly larger than the ones used in this study [44]. While determining the fundamental processes that limit battery performance is a challenging task, this paper shows how for appropriate systems that neutron imaging can provide significant insights.

4. Conclusions

This report described in situ neutron imaging experiments to track the lithiation/delithiation of a Li-ion battery full cell, where the electrodes were comprised of sintered active materials. Although the pixel size for neutron imaging is relatively large, the use of thick sintered electrode containing only active material enabled multiple data points through the depth of each electrode to be tracked during the discharge process, when highly attenuating Li + was transferred from the anode to the cathode. Comparison was made between the experimentally obtained relative transmission profiles and calculations of the total Li concentration at different depths in the cell. The calculations and experiments showed good qualitative agreement for the two cells investigated, capturing the more uniform lithiation of the LCO electrode during discharge, a delithiation front that propagated from the separator towards the current collector in the LTO electrode, and delithiation that started near the LTO current collector in the thicker LTO/ LCO cell. Future efforts to more quantitatively match experiment and calculation will be needed, and such efforts will require improvements in both. For example, higher resolution neutron imaging in the order of 10 µm, coupled with improved alignment, will reduce perceived gradients in regions near the edges of the electrode. The improvements in resolution generally will require a tradeoff with regards to acquisition time and field-of-view [20]. Also, improvements in accuracy of the electronic conductivity of the active material, in particular as a function

of different states of lithiation, coupled with estimation of the resistance associated with electron transfer between particle constituents, will greatly improve the accuracy of the matrix electronic conductivity polarization in the model. This study demonstrates the value in using neutron experiments to confirm lithiation/delithiation processes within Li-ion battery cells, which informs rational designs to improve upon the limiting steps in the system.

Acknowledgements

Funding is acknowledged from the National Science Foundation, grants CMMI-1825216 and CBET-1652488. This research used resources at the High Flux Isotope Reactor and Spallation Neutron Source, a DOE Office of Science User Facility operated by the Oak Ridge National Laboratory.

Appendix A. Supplementary data

Supplementary data to this article can be found online at https://doi.org/10.1016/j.jpowsour.2019.02.075.

References

- J.M. Tarascon, M. Armand, Issues and challenges facing rechargeable lithium batteries, Nature 414 (2001) 359–367 https://doi.org/10.1142/9789814317665_
- [2] S. Passerini, B. Scrosati, Lithium and lithium-ion batteries: challenges and prospects, Electrochem. Soc. Interface 25 (2016) 85–87 https://doi.org/10.1149/2. F09163if.
- [3] J.Y. Huang, L. Zhong, C.M. Wang, J.P. Sullivan, W. Xu, L.Q. Zhang, S.X. Mao, N.S. Hudak, X.H. Liu, A. Subramanian, H. Fan, In situ observation of the electrochemical lithiation of a single SnO₂ nanowire electrode, Science 330 (2010) 1515–1520 https://doi.org/10.1126/science.1195628.
- [4] J.N. Reimers, J.R. Dahn, Electrochemical and in situ X-ray diffraction studies of lithium intercalation in Li_xCoO₂, J. Electrochem. Soc. 139 (1992) 2091–2097 https://doi.org/10.1149/1.2221184.
- [5] M. Ebner, D.W. Chung, R.E. García, V. Wood, Tortuosity anisotropy in lithium-ion battery electrodes, Adv. Energy Mater. 4 (2014) 1301278 https://doi.org/10.1002/ aenm.201301278.
- [6] K.G. Gallagher, S.E. Trask, C. Bauer, T. Woehrle, S.F. Lux, M. Tschech, P. Lamp, B.J. Polzin, S. Ha, B. Long, Q. Wu, Optimizing areal capacities through understanding the limitations of lithium-ion electrodes, J. Electrochem. Soc. 163 (2016) A138–A149 https://doi.org/10.1149/2.0321602jes.
- [7] D. Takamatsu, A. Yoneyama, Y. Asari, T. Hirano, Quantitative visualization of salt concentration distributions in lithium-ion battery electrolytes during battery operation using X-ray phase imaging, J. Am. Chem. Soc. 140 (2018) 1608–1611 https://doi.org/10.1021/jacs.7b13357.
- [8] J. Wang, Y.C.K. Chen-Wiegart, J. Wang, In situ three-dimensional synchrotron X-ray nanotomography of the (de) lithiation processes in tin anodes, Angew. Chem. Int. Ed. 53 (2014) 4460–4464 https://doi.org/10.1002/anie.201310402.
- [9] H. Zhou, K. An, S. Allu, S. Pannala, J. Li, H.Z. Bilheux, S.K. Martha, J. Nanda, Probing multiscale transport and inhomogeneity in a lithium-ion pouch cell using in situ neutron methods, ACS Energy Lett 1 (2016) 981–986 https://doi.org/10.1021/ acsenergylett.6b00353.
- [10] J.B. Siegel, X. Lin, A.G. Stefanopoulou, D.S. Hussey, D.L. Jacobson, D. Gorsich, Neutron imaging of lithium concentration in LFP pouch cell battery, J. Electrochem. Soc. 158 (2011) A523–A529 https://doi.org/10.1149/1.3566341.
- [11] Y. Zhang, K.R. Chandran, H.Z. Bilheux, Imaging of the Li spatial distribution within V₂O₅ cathode in a coin cell by neutron computed tomography, J. Power Sources 376 (2018) 125–130 https://doi.org/10.1016/j.jpowsour.2017.11.080.
- (2018) 125–130 https://doi.org/10.1016/j.jpowsour.2017.11.080.
 [12] M. Singh, J. Kaiser, H. Hahn, Thick electrodes for high energy lithium ion batteries, J. Electrochem. Soc. 162 (2015) A1196–A1201 https://doi.org/10.1149/2. 0401507ies
- [13] J.P. Robinson, J.J. Ruppert, H. Dong, G.M. Koenig, Sintered electrode full cells for high energy density lithium-ion batteries, J. Appl. Electrochem. 48 (2018) 1297–1304 https://doi.org/10.1007/s10800-018-1242-y.
- [14] W. Lai, C.K. Erdonmez, T.F. Marinis, C.K. Bjune, N.J. Dudney, F. Xu, R. Wartena, Y.M. Chiang, Ultrahigh-energy-density microbatteries enabled by new electrode architecture and micropackaging design, Adv. Mater. 22 (2010) E139–E144 https://doi.org/10.1002/adma.200903650.
- [15] M. Doyle, T.F. Fuller, J. Newman, Modeling of galvanostatic charge and discharge of the lithium/polymer/insertion cell, J. Electrochem. Soc. 140 (1993) 1526–1533 https://doi.org/10.1149/1.2221597.
- [16] T.F. Fuller, M. Doyle, J. Newman, Simulation and optimization of the dual lithium ion insertion cell, J. Electrochem. Soc. 141 (1994) 1–10 https://doi.org/10.1149/1. 2054684
- [17] T.F. Fuller, M. Doyle, J. Newman, Relaxation phenomena in lithium-ion-insertion cells, J. Electrochem. Soc. 141 (1994) 982–990 https://doi.org/10.1149/1. 2054969

- [18] Z. Qi, G.M. Koenig Jr., High-performance LiCoO₂ sub-micrometer materials from scalable microparticle template processing, ChemistrySelect 1 (2016) 3992–3999 https://doi.org/10.1002/slct.201600872.
- [19] Z. Qi, G.M. Koenig, A carbon-free lithium-ion solid dispersion redox couple with low viscosity for redox flow batteries, J. Power Sources 323 (2016) 97–106 https://doi.org/10.1016/j.jpowsour.2016.05.033.
- [20] L. Santodonato, H. Bilheux, B. Bailey, J. Bilheux, P. Nguyen, A. Tremsin, D. Selby, L. Walker, The CG-1D neutron imaging beamline at the Oak Ridge National Laboratory high flux isotope reactor, Physics Procedia 69 (2015) 104–108 https://doi.org/10.1016/j.phpro.2015.07.015.
- [21] J. Versieck, J. Hoste, F. Barbier, H. Steyaert, J. De Rudder, H. Michels, Determination of chromium and cobalt in human serum by neutron activation analysis, Clin. Chem. 24 (1978) 303–308.
- [22] M. Wagner, H. Vonach, A. Pavlik, B. Strohmaier, S. Tagesen, J. Martinez Rico, Evaluation of Cross Sections for 14 Important Neutron Dosimetry Reactions, Physik Daten (Physics Data) No.13-5, Fachinformationszentrum, Karlsruhe, Germany, 1990
- [23] P. Albertus, J. Newman, Introduction to dualfoil 5.0, University of California Berkeley, Berkeley, CA, 2007 Tech. Rep.
- [24] S. Allu, S. Kalnaus, W. Elwasif, S. Simunovic, J.A. Turner, S. Pannala, A new open computational framework for highly-resolved coupled three-dimensional multiphysics simulations of Li-ion cells, J. Power Sources 246 (2014) 876–886 https:// doi.org/10.1016/j.jpowsour.2013.08.040.
- [25] N. Nitta, F. Wu, J.T. Lee, G. Yushin, Li-ion battery materials: present and future, Mater. Today 18 (2015) 252–264 https://doi.org/10.1016/j.mattod.2014.10.040.
 [26] A. Du Pasquier, I. Plitz, S. Menocal, G. Amatucci, A comparative study of Li-ion
- [26] A. Du Pasquier, I. Plitz, S. Menocal, G. Amatucci, A comparative study of Li-ion battery, supercapacitor and nonaqueous asymmetric hybrid devices for automotive applications, J. Power Sources 115 (2003) 171–178 https://doi.org/10.1016/ S0378-7753(02)00718-8.
- [27] H. Zheng, J. Li, X. Song, G. Liu, V.S. Battaglia, A comprehensive understanding of electrode thickness effects on the electrochemical performances of Li-ion battery cathodes, Electrochim. Acta 71 (2012) 258–265 https://doi.org/10.1016/j. electacta.2012.03.161.
- [28] R. Moshtev, B. Johnson, State of the art of commercial Li ion batteries, J. Power Sources 91 (2000) 86–91 https://doi.org/10.1016/S0378-7753(00)00458-4.
- [29] M. Rashid, A. Sahoo, A. Gupta, Y. Sharma, Numerical modelling of transport limitations in lithium titanate anodes, Electrochim. Acta 283 (2018) 313–326 https://doi.org/10.1016/j.electacta.2018.06.147.
- [30] M. Ménétrier, I. Saadoune, S. Levasseur, C. Delmas, The insulator-metal transition upon lithium deintercalation from LiCoO₂: electronic properties and ⁷Li NMR study, J. Mater. Chem. 9 (1999) 1135–1140 https://doi.org/10.1039/A900016J.
- [31] D. Young, A. Ransil, R. Amin, Z. Li, Y.M. Chiang, Electronic conductivity in the Li₄/₃Ti_{5/3}O₄-Li_{7/3}Ti_{5/3}O₄ system and variation with state-of-charge as a Li battery anode, Adv. Energy Mater 3 (2013) 1125–1129 https://doi.org/10.1002/aenm. 201300134.
- [32] K. Zaghib, M. Simoneau, M. Armand, M. Gauthier, Electrochemical study of Li₄Ti₅O₁₂ as negative electrode for Li-ion polymer rechargeable batteries, J. Power Sources 81 (1999) 300–305, https://doi.org/10.1016/50378-7753(99))00200-8
- Sources 81 (1999) 300–305 https://doi.org/10.1016/S0378-7753(99)00209-8.
 [33] L. Geng, M.E. Denecke, S.B. Foley, H. Dong, Z. Qi, G.M. Koenig, Electrochemical characterization of lithium cobalt oxide within aqueous flow suspensions as an indicator of rate capability in lithium-ion battery electrodes, Electrochim. Acta 281 (2018) 822–830 https://doi.org/10.1016/j.electacta.2018.06.037.
- [34] K. Kataoka, Y. Takahashi, N. Kijima, J. Akimoto, K.I. Ohshima, Single crystal growth and structure refinement of Li₄Ti₅O₁₂, J. Phys. Chem. Solid. 69 (2008) 1454–1456 https://doi.org/10.1016/j.jpcs.2007.10.134.
 [35] Y. Takahashi, N. Kijima, K. Dokko, M. Nishizawa, I. Uchida, J. Akimoto, Structure
- [35] Y. Takahashi, N. Kijima, K. Dokko, M. Nishizawa, I. Uchida, J. Akimoto, Structure and electron density analysis of electrochemically and chemically delithiated LiCoO₂ single crystals, J. Solid State Chem. 180 (2007) 313–321 https://doi.org/ 10.1016/j.issc.2006.10.018
- [36] Z. He, Z. Wang, F. Wu, H. Guo, X. Li, X. Xiong, Spherical Li₄Ti₅O₁₂ synthesized by spray drying from a different kind of solution, J. Alloy. Comp. 540 (2012) 39–45 https://doi.org/10.1016/j.jallcom.2012.06.044.
- [37] Q. Zhang, Q. Guo, R.E. White, Semi-empirical modeling of charge and discharge profiles for a LiCoO₂ electrode, J. Power Sources 165 (2007) 427–435 https://doi. org/10.1016/j.jpowsour.2006.12.025.
- [38] M. Park, X. Zhang, M. Chung, G.B. Less, A.M. Sastry, A review of conduction phenomena in Li-ion batteries, J. Power Sources 195 (2010) 7904–7929 https:// doi.org/10.1016/j.jpowsour.2010.06.060.
- [39] J. Nanda, H. Bilheux, S. Voisin, G.M. Veith, R. Archibald, L. Walker, S. Allu, N.J. Dudney, S. Pannala, Anomalous discharge product distribution in lithium-air cathodes, J. Phys. Chem. C 116 (2012) 8401–8408 https://doi.org/10.1021/ jp3016003.
- [40] J. Landesfeind, A. Eldiven, H.A. Gasteiger, Influence of the binder on lithium ion battery electrode tortuosity and performance, J. Electrochem. Soc. 165 (2018) A1122–A1128 https://doi.org/10.1149/2.0971805jes.
 [41] J. Chen, J. Liu, Y. Qi, T. Sun, X. Li, Unveiling the roles of binder in the mechanical
- [41] J. Chen, J. Liu, Y. Qi, T. Sun, X. Li, Unveiling the roles of binder in the mechanical integrity of electrodes for lithium-ion batteries, J. Electrochem. Soc. 160 (2013) A1502–A1509 https://doi.org/10.1149/2.088309jes.
- [42] C.L. Cobb, C.J. Bae, Tortuosity of binder-free and carbon-free high energy density LiCoO₂ electrodes for rechargeable lithium-ion batteries, ECS Trans 58 (2014) 13–24 https://doi.org/10.1149/05813.0013ecst.
- [43] I.V. Thorat, D.E. Stephenson, N.A. Zacharias, K. Zaghib, J.N. Harb, D.R. Wheeler, Quantifying tortuosity in porous Li-ion battery materials, J. Power Sources 188 (2009) 592–600 https://doi.org/10.1016/j.jpowsour.2008.12.032.
- [44] K.G. Gallagher, P.A. Nelson, D.W. Dees, Simplified calculation of the area specific impedance for battery design, J. Power Sources 196 (2011) 2289–2297 https://doi. org/10.1016/j.jpowsour.2010.10.020.